Spinning Meta-Cam: Spectro-Polarimetric Long-wave Infrared Thermal Imaging based on Spinning Metasurfaces

XUEJI WANG,[1] ZIYI YANG,[1] FANGLIN BAO,[1],TYLER SENTZ,[1] AND ZUBIN JACOB[1],*

[1]*Elmore Family School of Electrical and Computer Engineering, Purdue University, West Lafayette, IN 47907*
*[*]*zjacob@purdue.edu*

Abstract: Spectro-polarimetric imaging in the long-wave infrared (LWIR) region is a powerful tool for capturing temperature, material composition, and surface morphology information. However, current spectro-polarimetric LWIR imagers are often bulky and severely limited in spectral resolution and field of view (FOV). In this work, we present a new paradigm for spectro-polarimetric demultiplexing by combining large-area meta-optical devices and advanced computational imaging algorithms. We use the intrinsic dispersion and polarization modulation of anisotropic spinning metasurfaces to achieve simultaneous spectral and polarimetric resolution without the need for bulky filter wheels or interferometers. Our spinning-metasurface-based spectro-polarimetric module is robust, compact (< 10 x 10 x 10 cm) and has a wide field of view (25°). Our approach represents a significant advancement in the field of thermal imaging, allowing for high-quality, information-rich thermal image data for a wide range of applications such as astronomical exploration, medical diagnosis, and agricultural monitoring.

1. Introduction

Advances in machine vision technology have spurred a need for high-resolution, informative images across a range of applications scenarios [1–4]. Infrared thermography is a powerful tool for capturing temperature, material composition, and surface morphology information about objects, even in situations with limited external lighting [5]. The long-wave infrared (LWIR) spectral region is particularly useful for infrared thermography as most room-temperature objects emit thermal radiation at these wavelengths, according to Planck's law. Additionally, the LWIR atmospheric transmission window reduces the effect of environmental turbulence on the thermal radiation signal in this region (Fig. 1a). As a result, LWIR thermal imaging has become a crucial technology frontier in various applications such as astronomical exploration [6, 7], medical diagnosis [8], and agricultural monitoring [9].

Furthermore, demultiplexing the LWIR thermal radiation into its spectral and polarimetric components has been heralded as the next-generation solution for applications such as methane sensing [10] and thermal facial recognition [11]. However, the commonly used mosaic filter approach for spectral demultiplexing [12–16] is not practical for LWIR thermal imaging, due to the limited number of pixels in LWIR focal plane arrays (Fig. 1b). State-of-the-art LWIR spectral imagers instead rely on infrared bandpass filters (Fig. 1c) or interferometry (Fig. 1d), but these methods have limitations such as bulky filter wheels with limited spectral resolution, or unrobust interferometers with a limited field of view (FOV). Recently, metasurface-based spectral and polarimetric imaging has demonstrated huge potential in the visible region of spectrum [17–19], but using infrared metasurfaces in LWIR thermal imaging is still an open technological frontier. We emphasize that directly integrating metasurfaces on a thermal sensor significantly changes the heat transport properties of the sensor and make this approach incompatible with the widely
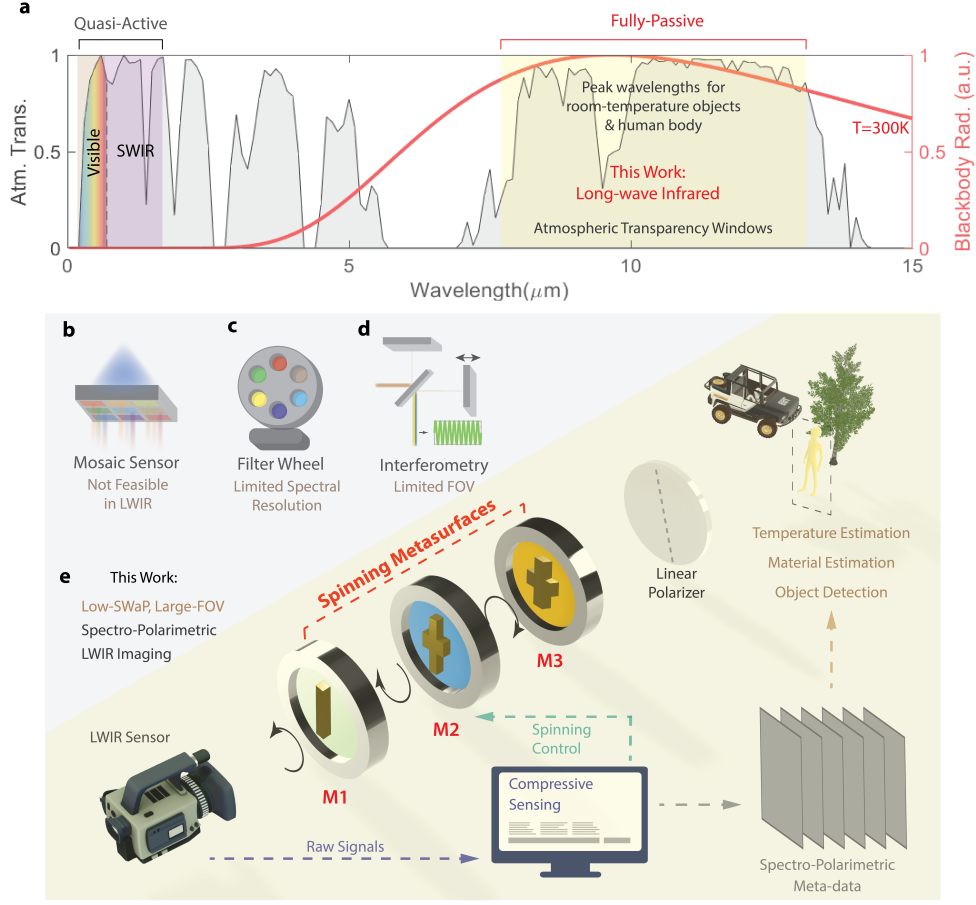
Fig. 1. Long-wave infrared (LWIR) spectro-polarimetric thermal imaging. (a) The room-temperature blackbody radiation (shown in red) and the atmospheric transmission spectrum (shown as a shaded area). The LWIR spectral region is crucial for thermal imaging due to its peaked room-temperature thermal radiation spectrum and the atmospheric transparency window. (b-d) Conventional methods for spectral imaging, such as using a mosaic sensor (b), a filter wheel (c), or interferometry (d), either pose limitations or are infeasible for LWIR thermal imaging. (e) In this study, we propose a new approach for spectro-polarimetric thermal imaging, achieved by combining large-area spinning metasurfaces and compressive sensing reconstruction algorithms

adopted microbolometer technology in LWIR thermal imaging.

To address these limitations, in this work, we put forth a new paradigm for spectro-polarimetric thermal imaging using large-area meta-optics. The spectral demultiplexing is achieved through the intrinsic dispersion and polarization modulation in anisotropic metasurfaces, and spectral reconstruction is realized using compressive sensing and dictionary learning algorithms. Our designs employ simple 2D structures with large feature sizes ($> 1\mu m$), which can be easily made by standard photo-lithography techniques, enabling large-area fabrication and scalable manufacturing. Our demonstration provides a new technical route to solve the long-standing issue of robust and portable thermal imaging with simultaneous spectral and polarimetric resolution. By utilizing meta-optical designs and advanced computational imaging methods, our approach

offers a promising platform for next-generation high-contrast LWIR thermal imaging.

The architecture of our spinning-metasurface based spectro-polarimetric imaging system is depicted in Fig. 1e. It comprises of a broadband linear polarizer, three anisotropic and dispersive metasurfaces, and an LWIR imaging sensor. The polarizer is utilized to polarize the incoming thermal radiation signals, and the metasurfaces are utilized to realize spectral filtering. We design the metasurfaces with high anisotropy to produce distinct spectral responses for orthogonal polarizations. Additionally, the metasurfaces' dispersion rotates different wavelengths of light to varying polarization orientations. By using the metasurfaces in tandem and axially spinning the polarizer and metasurfaces to different angles, we obtain tunable transmission spectra that sample the incident thermal radiation in its spectral and polarimetric channels. We then reconstruct unknown spectra of imaging targets using compressive sensing and dictionary learning algorithms. Dictionary learning generates a set of basis functions that represent the unknown spectra in a sparse format [20]. Compressed sensing enables accurate reconstruction of the sparse spectra from limited number of measurements [21]. Combining these two techniques enables accurate and stable spectral reconstruction in the presence of noise and measurement errors [22]. The four-dimensional spectro-polarimetric data generated by our system offers a wealth of physical information about an imaging target, making it a valuable tool for physics-driven machine vision [4, 23], facilitating various tasks such as object detection and semantic segmentation [24, 25].

2. Design of Spinning Metasurfaces

To quantitatively describe the mechanism of the spinning-angle-controlled transmission spectra, we represent the spectro-polarimetric response of the metasurfaces using Jones matrices. Assuming that the transmission axis (x-axis) of the input linear polarizer is at 0 degrees, the Jones matrix J_i of a metasurface i with the x-axis at a spinning angle θ_i can be expressed as:

$$J_i(\theta_i, \lambda) = R(-\theta_i) \cdot J_{M_i}(\lambda) \cdot R(\theta_i)$$

$$= \begin{bmatrix} cos(\theta_i) & -sin(\theta_i) \\ sin(\theta_i) & cos(\theta_i) \end{bmatrix} \begin{bmatrix} t_{ip}(\lambda) & 0 \\ 0 & t_{is}(\lambda) \end{bmatrix} \begin{bmatrix} cos(\theta_i) & sin(\theta_i) \\ -sin(\theta_i) & cos(\theta_i) \end{bmatrix} \quad (1)$$

where R is the rotation matrix, J_{Mi} contains the anisotropic transmission of the metasurface t_{ip} and t_{is} along the two principle axes p and s. Then, the Jones matrix of the three-metasurface assembly is given by:

$$J(\theta_1, \theta_2, \theta_3, \lambda) = J_1(\theta_1, \lambda) \cdot J_2(\theta_2, \lambda) \cdot J_3(\theta_3, \lambda) \cdot \quad (2)$$

Thus, the total transmission spectrum of the three spinning metasurfaces strongly depends on the spinning-angle-combinations $\Theta = (\theta_1, \theta_2, \theta_3)$ when the constituted metasurfaces are strongly anisotropic and dispersive, i.e. $t_{ip}(\lambda) \neq t_{is}(\lambda)$ (see Supplementary Materials for the detailed analysis). We note that large differences between the spectral responses of the three metasurfaces (M1, M2, M3) are also introduced to minimize the correlations between the generated spectra, which can significantly improve the spectral reconstruction performance [26]. We emphasize that our design generates a large set of distinct transmission spectra with only three metasurfaces, while the total number of spectra in traditional mosaic array is limited to the number of metasurfaces/filters used [12–18].

Accordingly, we design the metasurfaces and experimentally achieve three key characteristics for optimized spectro-polarimetric imaging performance: 1) Strong anisotropy and dispersion for efficient wavelength demultiplexing; 2) High transmission and low self-emission for high signal to noise ratio (SNR); 3) Small angular dependence for a large FOV. The unit cell of the three designed metasurfaces are shown in Fig. 2 a-c. Strong dispersive anisotropy of the transmission
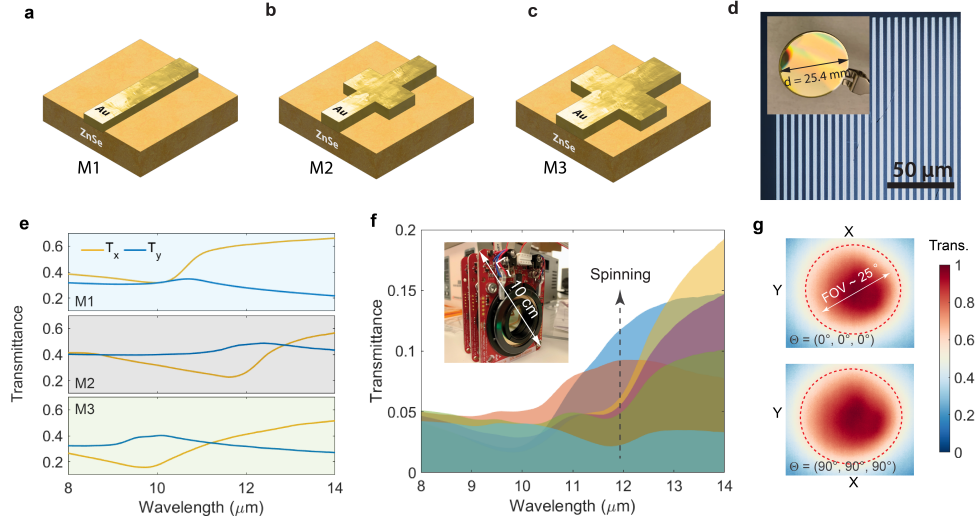
Fig. 2. Design and characterization of the spinning metasurfaces. (a-c) Schematics of the three different metasurface devices. (d) A scanning electron microscope (SEM) image of a fabricated metasurface. Inset: an optical image of a 1-inch-diameter device used for the imaging experiments, highlighting the large-area uniformity. (e) The measured polarized transmission spectra (t_{ip} and t_{is}) of the three metasurfaces (M1 - M3) are depicted, displaying strong anisotropy and distinctive dispersion. (f) The tunable transmission spectra controlled by the spinning angle combinations of the three metasurfaces. Inset: an optical image of the motorized rotary mount. The overall size of the spinning metasurface module is smaller than 10 cm x 10 cm x 10 cm, making it a promising platform for next-generation high-contrast LWIR thermal imaging. (g) The normalized spatial transmittance of the module at two representative spinning angle combinations $\Theta = (0°, 0°, 0°)$ (top) and $\Theta = (90°, 90°, 90°)$ (bottom). The red circles correspond to a transmittance of 0.5 and the field of view of the imaging system is estimated to be 25°.

spectra can be observed in Fig. 2e. Additionally, we emphasize that large-area devices are generally required for imaging applications to ensure sufficient numerical aperture. All the metasurfaces designed here have feature sizes larger than 1 μm. Large-area devices (25.4mm in diameter) with high structural quality and uniformity (Fig. 2d) can be rapidly fabricated by standard photo-lithography techniques, enabling scalable manufacturing for practical applications. This is in strong contrast to recent works on miniaturized spectrometers [27–35], where the device footprint is on the micrometer scale and thus not suitable for imaging applications.

The tunable transmission spectra produced by our spinning metasurfaces are shown in Fig. 2f. The distinct spectra are a result of the tuned spinning-angle combination Θ. We integrate the three fabricated metasurfaces tandemly via compact rotary mounts to independently control the rotation of each metasurface (Inset of Fig. 2g). We also optimize the spinning-angle combinations of the three spinning metasurfaces using genetic algorithms to generate largely uncorrelated transmission spectra for optimal spectral reconstruction performance (see Supplementary Materials for details). Additionally, we note that increasing the number of metasurfaces can further improve the spectral resolution, but simultaneously reduces the SNR as the peak transmissions of the LWIR devices are limited to around 0.6. However, our method has the potential to scale up into the hyperspectral regime by adding more high-transmission LWIR metasurfaces.

We also evaluate the FOV of our imaging module by integrating it with an LWIR thermal camera and capturing images of a large area uniform blackbody. To determine the spatial transmission efficiency, we normalize the signal counts of each pixel by the counts at the center of the images. We also define the angular range with transmittance above 0.5 as the effective FOV of a system. As seen in Figure 2g, our spinning metasurface module has an FOV of around 25 degrees, which is significantly larger than what can be achieved with interferometer-based spectral imagers.
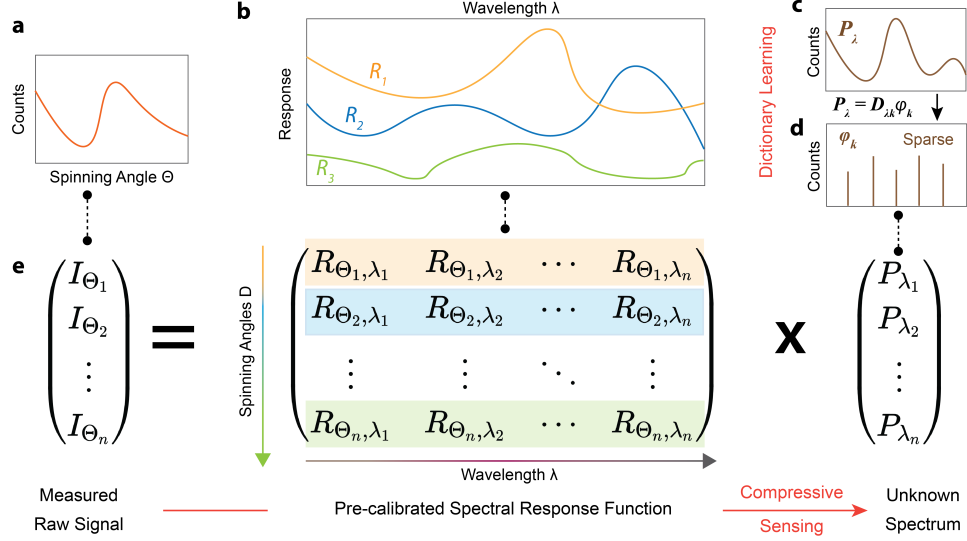
3. Spectral Reconstruction

Fig. 3. Schematic of the spectral reconstruction process. The measured raw signal (a) can be expressed by the pre-calibrated spectral response function (b) of the imaging system multiplied by the spectrum of an imaging target (c). For the spectral reconstrcution, the unknown spectrum P_λ is projected onto a sparse representation basis $D_{k\lambda}$ using dictionary learning (c and d). This sparse representation ϕ_k is then used for compressive sensing based reconstruction (e). The use of compressive sensing and dictionary learning in the reconstruction process significantly improves the reconstruction accuracy, making the spinning-metasurface-based spectro-polarimetric imaging more robust against noise and measurement errors.

To extract the unknown spectro-polarimetric properties of various imaging targets, we use a combination of dictionary learning and compressive sensing algorithms in the reconstruction process. The tunable transmission spectra produced by our spinning metasurfaces (shown in Fig. 2g) are not narrowband, which means that the collected raw signals at different spinning-angle combinations Θ do not directly reflect the spectral radiance at different wavelengths. Instead, the collected signal $I(\Theta)$ at each pixel can be described as an integral of the spectral response function $R(\Theta, \lambda)$ multiplied by the ground truth spectrum $P(\lambda)$ that we wish to obtain, i.e. $I(\Theta) = \int_{\lambda_{\min}}^{\lambda_{\max}} R(\Theta, \lambda)P(\lambda)\mathrm{d}\lambda$. To solve for this equation, we discretize the spectral range of interest and express it in a tensor form as shown in Eq. 3:

$$I_\Theta = R_{\Theta\lambda}P_\lambda \tag{3}$$

We emphasize that directly solving Eq. 3 does not produce accurate spectral reconstructions. In theory, we can use measured signals I_Θ and the pre-calibrated response function $R_{\theta\lambda}$ to determine unknown spectra P_λ at each pixel of a scene. However, in practice, two limitations impede the performance of spectral reconstruction: the problem becomes underdetermined when there are many discretized wavelength bands, and measurement noise affects both I_Θ and $R_{\Theta\lambda}$, making the direct reconstruction method unstable and the results inaccurate.

To improve the accuracy and stability of spectral reconstruction, we use compressed sensing and dictionary learning algorithms to solve Eq. 3. Specifically, we first use dictionary learning to create a dictionary of basis functions D. These functions can represent any thermal radiation spectrum in the space of spectra we are studying. We then project the unknown spectrum P_λ as a linear combination of the basis functions in the dictionary (Fig. 3 b and c). We have,

$$P_\lambda = D_{\lambda k}\phi_k \tag{4}$$

where ϕ_k is known as a sparse coding of the spectrum P_λ. With this sparse representation, the spectral reconstruction problem can be solved by first obtaining ϕ_{recon}:

$$\begin{aligned}\phi_{\text{recon}} &= \arg\min_{\phi_k}\|\phi_k\|_1 \\ \text{s.t. } \|I_\Theta - R_{\Theta\lambda}P_\lambda\|_2 &= \|I_P - A_{\Theta k}\phi_k\|_2 < \epsilon\end{aligned} \tag{5}$$

where $A_{\Theta k} = R_{\Theta\lambda}D_{\lambda k}$, and ϵ is the residual error. Finally, the spectra P_λ at each pixel of a scene is reconstructed by

$$P_{\text{recon}} = D_{\lambda k}\phi_{\text{recon}} \tag{6}$$

Our reconstruction method significantly improves the reconstruction accuracy, making the spinning-metasurface-based spectro-polarimetric imaging more robust against noise and measurement errors.

4. Spectro-Polarimetric Imaging

To evaluate the performance of our prototype imaging system, we conduct experiments using a custom-designed 'PURDUE' target made of letters constructed from titanium and a glass substrate (Fig. 4a). Each letter has unique micro-grating structures (Inset of Fig. 4a) that generate distinctive polarimetric signatures in the thermal radiation signal. The glass substrate also features a characteristic emission peak around 11 μm. Note that we heat the image target to $150°C$ to generate high signal intensity. The reconstructed spectra of four representative pixels are shown in Fig. 4 b-e. We compare them with the ground truth spectra measured by a Fourier-transform infrared spectrometer, validating the effectiveness of our reconstruction approach. The reconstructed spectral frames (Fig. 2 f) also exhibit high contrasts between different wavelengths, demonstrating that the system can effectively reveal the LWIR spectral properties of different targets. We note that the relatively low reconstruction accuracy at shorter wavelengths (8 - 10 μm) results from the low transmission (low SNR) and the high correlation (similarity) between the tuned spectra (Fig. 2f).

We also obtain the polarimetric information including degree the linear polarization (DOLP) and the angle of linear polarization (AoLP) using the designed system. For polarimetric imaging, we collectively rotate the spinning metasurfaces and the input polarizer, selecting four different polarizations ($0°$, $90°$, $45°$ and $-45°$) while maintaining the same spectral transmission. We use the first three Stokes parameters to quantify the polarimetric information associated with each pixel, i.e. $S_0 = I_0 + I_{90}$, $S_1 = I_0 - I_{90}$, and $S_2 = I_{45} - I_{-45}$, where I_0, I_{90}, I_{45} and I_{-45} are the light intensity at polarization angles of $0°$, $90°$, $45°$ and $-45°$, respectively. The DoLP and AoLP are then calculated at each wavelength through DoLP $= \sqrt{S_1^2 + S_2^2}/S_0$ and
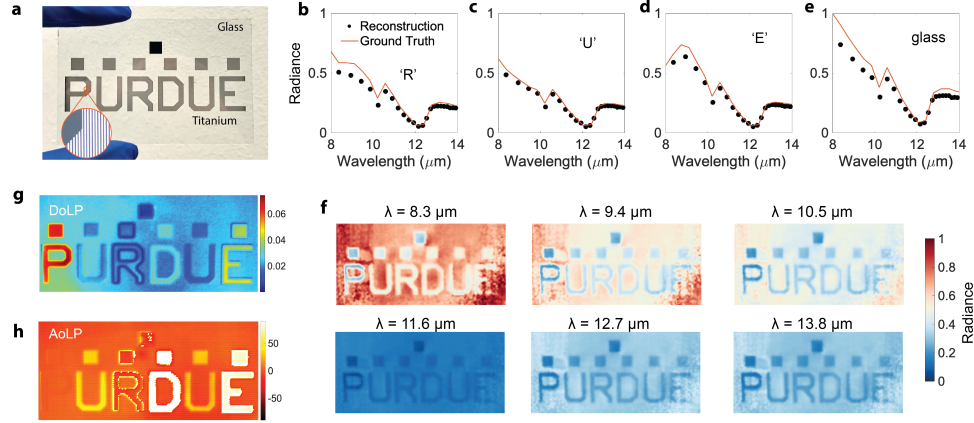
Fig. 4. Spectro-polarimetric thermal imaging results. (a) An optical image of the 'PURDUE' imaging target that is constructed from titanium letters on a glass substrate. Inset: a zoomed-in optical image of the micro-structures in the letters, which generate distinctive spectral and polarimetric signatures. (b-e) Reconstructed spectra of four representative pixels (corresponding to the letter 'R', 'U', 'E' and the glass substrate, respectively) compared with the ground truth spectra measured by a Fourier-transform infrared spectrometer. (f) Reconstructed spectral frames at 6 representative wavelengths. The contrast between different frames demonstrates that the system can effectively reveal the LWIR spectral properties of various materials and structures. (g-h) Degree-of-linear-polarization and angle-of-linear-polarization frames. Distinctive polarimetric signatures can be observed for each letter in the images.

AoLP = $arctan(S_2/S_1)$. As shown in Fig. 4 h and i, we can clearly distinguish between different letters based on their polarimetric signatures in the thermal radiation signal. The four-dimensional spatial-spectro-polarimetric data-tesseract provides significantly more insight associated with an object, making it a powerful tool for a wide range of imaging applications.

5. Conclusion

Our results provide an innovative approach for spectro-polarimetric thermal imaging by combining meta-optics and computational imaging. The low-SWaP (size, weight, and power) system opens the door for physics-driven machine vision. The high-dimensional thermal image data can significantly improve the performance of tasks such as depth estimation, object detection, and semantic segmentation when only radiative heat signal is available. Furthermore, we foresee that spectro-polarimetric thermal imaging can also be a powerful tool for scientific research, allowing for non-destructive characterization in the infrared region to investigate a wide range of novel physical phenomena, such as anisotropic thermal conduction [36] and directional radiative heat transfer [37]. Overall, our work provides a key development in the rapidly growing field of thermal imaging.

Disclosures. The authors declare no conflicts of interest.

Data availability. Data underlying the results presented in this paper are not publicly available at this time but may be obtained from the authors upon reasonable request.

Supplemental document. See Supplementary Materials for supporting content.

6. References

References

1. A. M. Valm, S. Cohen, W. R. Legant, J. Melunis, U. Hershberg, E. Wait, A. R. Cohen, M. W. Davidson, E. Betzig, and J. Lippincott-Schwartz, "Applying systems-level spectral imaging and analysis to reveal the organelle interactome," Nature **546**, 162–167 (2017).
2. M. C. Martin, C. Dabat-Blondeau, M. Unger, J. Sedlmair, D. Y. Parkinson, H. A. Bechtel, B. Illman, J. M. Castro, M. Keiluweit, D. Buschke *et al.*, "3D spectral imaging with synchrotron fourier transform infrared spectro-microtomography," Nat. Methods **10**, 861–864 (2013).
3. Y. Ozeki, W. Umemura, Y. Otsuka, S. Satoh, H. Hashimoto, K. Sumimura, N. Nishizawa, K. Fukui, and K. Itoh, "High-speed molecular spectral imaging of tissue with stimulated raman scattering," Nat. Photon. **6**, 845–851 (2012).
4. G. E. Karniadakis, I. G. Kevrekidis, L. Lu, P. Perdikaris, S. Wang, and L. Yang, "Physics-informed machine learning," Nat. Rev. Phys. **3**, 422–440 (2021).
5. M. Vollmer, "Infrared thermal imaging," in *Computer Vision: A Reference Guide,* (Springer, 2021), pp. 666–670.
6. T. Okada, T. Fukuhara, S. Tanaka, M. Taguchi, T. Arai, H. Senshu, N. Sakatani, Y. Shimaki, H. Demura, Y. Ogawa *et al.*, "Highly porous nature of a primitive asteroid revealed by thermal imaging," Nature **579**, 518–522 (2020).
7. V. Gámez Rosas, J. W. Isbell, W. Jaffe, R. G. Petrov, J. H. Leftley, K.-H. Hofmann, F. Millour, L. Burtscher, K. Meisenheimer, A. Meilland *et al.*, "Thermal imaging of dust hiding the black hole in NGC 1068," Nature **602**, 403–407 (2022).
8. E. Ring and K. Ammer, "Infrared thermal imaging in medicine," Physiol. Meas. **33**, R33 (2012).
9. G. Messina and G. Modica, "Applications of UAV thermal imagery in precision agriculture: State of the art and future research outlook," Remote. Sens. **12**, 1491 (2020).
10. M. Gålfalk, G. Olofsson, P. Crill, and D. Bastviken, "Making methane visible," Nat. Clim. Chang. **6**, 426–430 (2016).
11. K. P. Gurton, A. J. Yuffa, and G. W. Videen, "Enhanced facial recognition for thermal imagery using polarimetric imaging," Opt. letters **39**, 3857–3859 (2014).
12. T. Xu, Y.-K. Wu, X. Luo, and L. J. Guo, "Plasmonic nanoresonators for high-resolution colour filtering and spectral imaging," Nat. Commun. **1**, 1–5 (2010).
13. F. Yesilkoy, E. R. Arvelo, Y. Jahani, M. Liu, A. Tittl, V. Cevher, Y. Kivshar, and H. Altug, "Ultrasensitive hyperspectral imaging and biodetection enabled by dielectric metasurfaces," Nat. Photon. **13**, 390–396 (2019).
14. J. Bao and M. G. Bawendi, "A colloidal quantum dot spectrometer," Nature **523**, 67–70 (2015).
15. Z. Wang, S. Yi, A. Chen, M. Zhou, T. S. Luk, A. James, J. Nogan, W. Ross, G. Joe, A. Shahsafi *et al.*, "Single-shot on-chip spectral sensors based on photonic crystal slabs," Nat. Commun. **10**, 1–6 (2019).
16. A. Tittl, A. Leitis, M. Liu, F. Yesilkoy, D.-Y. Choi, D. N. Neshev, Y. S. Kivshar, and H. Altug, "Imaging-based molecular barcoding with pixelated dielectric metasurfaces," Science **360**, 1105–1109 (2018).
17. A. McClung, S. Samudrala, M. Torfeh, M. Mansouree, and A. Arbabi, "Snapshot spectral imaging with parallel metasystems," Sci. Adv. **6**, eabc7646 (2020).
18. M. Makarenko, A. Burguete-Lopez, Q. Wang, F. Getman, S. Giancola, B. Ghanem, and A. Fratalocchi, "Real-time hyperspectral imaging in hardware via trained metasurface encoders," in *Proceedings of the IEEE/CVF Conference on Computer Vision and Pattern Recognition,* (2022), pp. 12692–12702.
19. N. A. Rubin, G. D'Aversa, P. Chevalier, Z. Shi, W. T. Chen, and F. Capasso, "Matrix fourier optics enables a compact full-stokes polarization camera," Science **365**, eaax1839 (2019).
20. K. Kreutz-Delgado, J. F. Murray, B. D. Rao, K. Engan, T.-W. Lee, and T. J. Sejnowski, "Dictionary learning algorithms for sparse representation," Neural Comput. **15**, 349–396 (2003).
21. E. J. Candès, J. Romberg, and T. Tao, "Robust uncertainty principles: Exact signal reconstruction from highly incomplete frequency information," IEEE Trans. Inf. Theory **52**, 489–509 (2006).
22. S. Zhang, Y. Dong, H. Fu, S.-L. Huang, and L. Zhang, "A spectral reconstruction algorithm of miniature spectrometer based on sparse optimization and dictionary learning," Sensors **18**, 644 (2018).
23. A. Signoroni, M. Savardi, A. Baronio, and S. Benini, "Deep learning meets hyperspectral image analysis: A multidisciplinary review," J. Imaging **5**, 52 (2019).
24. J. Lu, H. Liu, Y. Yao, S. Tao, Z. Tang, and J. Lu, "HSI road: A hyper spectral image dataset for road segmentation," in *2020 IEEE International Conference on Multimedia and Expo (ICME),* (IEEE, 2020), pp. 1–6.
25. K. Usmani, G. Krishnan, T. O'Connor, and B. Javidi, "Deep learning polarimetric three-dimensional integral imaging object recognition in adverse environmental conditions," Opt. Express **29**, 12215–12228 (2021).
26. Z. Wang and Z. Yu, "Spectral analysis based on compressive sensing in nanophotonic structures," Opt. Express **22**, 25608–25614 (2014).
27. Z. Yang, T. Albrow-Owen, W. Cai, and T. Hasan, "Miniaturization of optical spectrometers," Science **371**, eabe0722 (2021).
28. S. Yuan, D. Naveh, K. Watanabe, T. Taniguchi, and F. Xia, "A wavelength-scale black phosphorus spectrometer," Nat. Photon. **15**, 601–607 (2021).
29. H. H. Yoon, H. A. Fernandez, F. Nigmatulin, W. Cai, Z. Yang, H. Cui, F. Ahmed, X. Cui, M. G. Uddin, E. D. Minot *et al.*, "Miniaturized spectrometers with a tunable van der waals junction," Science **378**, 296–299 (2022).
30. Z. Yang, T. Albrow-Owen, H. Cui, J. Alexander-Webber, F. Gu, X. Wang, T.-C. Wu, M. Zhuge, C. Williams, P. Wang *et al.*, "Single-nanowire spectrometers," Science **365**, 1017–1020 (2019).

31. B. Redding, S. F. Liew, R. Sarma, and H. Cao, "Compact spectrometer based on a disordered photonic chip," Nat. Photon. **7**, 746–751 (2013).
32. R. Cheng, C.-L. Zou, X. Guo, S. Wang, X. Han, and H. X. Tang, "Broadband on-chip single-photon spectrometer," Nat. Commun. **10**, 1–7 (2019).
33. S. N. Zheng, J. Zou, H. Cai, J. Song, L. Chin, P. Liu, Z. Lin, D. Kwong, and A. Liu, "Microring resonator-assisted fourier transform spectrometer with enhanced resolution and large bandwidth in single chip solution," Nat. Commun. **10**, 1–8 (2019).
34. M. C. Souza, A. Grieco, N. C. Frateschi, and Y. Fainman, "Fourier transform spectrometer on silicon with thermo-optic non-linearity and dispersion correction," Nat. Commun. **9**, 1–8 (2018).
35. D. M. Kita, B. Miranda, D. Favela, D. Bono, J. Michon, H. Lin, T. Gu, and J. Hu, "High-performance and scalable on-chip digital fourier transform spectroscopy," Nat. Commun. **9**, 1–7 (2018).
36. S. Huang, M. Segovia, X. Yang, Y. R. Koh, Y. Wang, D. Y. Peide, W. Wu, A. Shakouri, X. Ruan, and X. Xu, "Anisotropic thermal conductivity in 2d tellurium," 2D Mater. **7**, 015008 (2019).
37. J. Xu, J. Mandal, and A. P. Raman, "Broadband directional control of thermal emission," Science **372**, 393–397 (2021).